

## Algebraic Reconstruction Techniques for Tomographic Particle Image Velocimetry

C. H. Atkinson and J. Soria

Laboratory for Turbulence Research in Aerospace and Combustion  
Department of Mechanical Engineering  
Monash University, Victoria, 3800 AUSTRALIA

### Abstract

Tomographic particle image velocimetry (Tomo-PIV) is a technique for three-component three-dimensional (3C-3D) velocity measurement based on the tomographic reconstruction of a volume intensity field from multiple two-dimensional projections. As such the performance and accuracy of this technique is highly dependant on the algorithm used for reconstruction. This paper presents an evaluation of four different tomographic reconstruction algorithms, namely multiplicative algebraic reconstruction technique (MART); adaptive algebraic reconstruction technique (AART); improved iterative algorithm for sparse object reconstruction (IIASOR); and simultaneous iterative reconstruction technique (SIRT). Results indicate that the MART and AART algorithms provide considerably better particle field reconstructions for fewer iterations.

### Introduction

Tomographic particle image velocimetry (Tomo-PIV) (4) is a recently introduced tool for three-component three-dimensional (3C-3D) velocity field measurements and has the potential to play an important role in the understanding of the complex 3D topology of turbulent flows. The technique is based on the tomographic reconstruction of instantaneous volumetric particle field intensity distributions from multiple simultaneous two-dimensional (2D) projections or views of the measurement volume. Reconstructed 3D intensity fields can then be three-dimensionally cross-correlated in 3D to determine the 3D particle displacements based on the same principles as standard planar PIV.

The reconstruction of an image or field from multiple projections dates back to Radon (12). The earliest applications appeared in the 1950s where radio astronomers used strip projections to reconstruct the distribution of radio emissions across celestial bodies (3), and was quickly adopted for medical diagnostics (11) in the form of computed axial tomography or CAT scans. The popularity of tomography stems from its non-intrusive nature and its use of standard two-dimensional measurement instruments. The widespread use of tomography in medical diagnostics, radio astronomy and geophysics has lead to the development of numerous reconstruction techniques that are optimised for various applications.

The application to transient fields such as fluid flows and heat transfer, represent a special case of reconstruction problems, owing to the need for the simultaneous recording of each projection. View angle limitations also become apparent in practical investigations where optical access to wind or water tunnels is often limited. For Tomo-PIV the reconstruction must also be able to resolve the multiple high intensity sources created by the scattering from numerous particles, while maintaining a low intensity background. This requirement is important for accurate cross-correlation based velocity extraction and is a departure from many medical applications, which tend to focus on the reconstruction of only one or two objects at a time. The processing time required for the reconstruction of the multiple large 3D

data sets needed to study turbulent statistics also requires highly efficient reconstruction algorithms, especially if Tomo-PIV is to become a standard laboratory tool. The algebraic family of reconstruction techniques appear particular suited to view-limited tomography, however the reconstruction quality can still vary greatly depending on the specific technique, relaxation parameters, number of iterations and projection quality.

This paper presents a comparison of different algebraic reconstruction algorithms towards the robust application of Tomo-PIV. The algorithms examined include the multiplicative algebraic reconstruction technique (MART) (6); adaptive algebraic reconstruction technique (AART) (10); improved iterative algorithm for sparse object reconstruction (IIASOR) (9); and simultaneous iterative reconstruction technique (SIRT) (6). Simulated data sets are used to compare of each reconstruction with a known particle field and thereby enable quantification of the reconstruction quality.

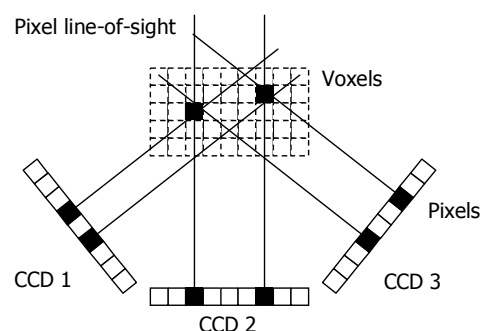


Figure 1: Schematic of multi-camera algebraic reconstruction technique. Filled voxels represent particle locations required to satisfy the filled pixels in each CCD recorded projection.

### Tomographic Reconstruction

In Tomo-PIV multiple CCD arrays are used to record projections of a common laser illuminated particle seeded fluid volume. The intensity recorded at each detector or pixel  $P_i$  on the CCD array, represents the integration of intensity through the illuminated volume along the pixel's line-of-sight  $s_i$ . A schematic of this is shown in figure 1. This can be expressed as:

$$P_i = \int_{-\infty}^{\infty} I(x, y, z) ds_i \quad (1)$$

where  $I(x, y, z)$  represents the unknown intensity source function. The goal of tomography is to invert the highly under determined integral equation from each projection to determine and hence reconstruct the intensity distribution within the volume.

Reconstruction techniques commonly reside in either the Fourier or spatial domain. Fourier techniques involving convolution are highly efficient and commonly used in medical diagnostics, yet in most cases require numerous equally spaced

projections that are unlikely to be realised in most fluid flow applications. A group of techniques that are better suited to limited view reconstruction are the algebraic reconstruction methods. These require the intensity volume be divided into a 3D grid of voxel elements as shown in figure 1. The integral along each pixel's line-of-sight can then be expressed in terms of a weighting matrix  $W_{ij}$ , which represent the contribution of each voxel's intensity to that recorded by each pixel:

$$P_i = \sum_j W_{ij} I_j \quad (2)$$

where  $I_j$  is a vector representing the intensity of each voxel. The contribution of each voxel to each pixel can be determined using relative volume intersection of a cylinder and a sphere (7) representing the pixel's line-of-sight and voxel, respectively. The intensity value in each voxel is then iteratively corrected such that the calculated projections of each voxel  $P_i$  approach the recorded intensity at each pixel. This iterative correction forms the basis of the algebraic reconstruction techniques, however the nature and implementation of this correction can vary significant and subsequently effect the convergence and quality of the reconstruction.

### Algebraic Reconstruction Algorithms

Four different iterative techniques are presented below, each being chosen for their ability to handle limited projections.

#### Multiplicative algebraic reconstruction technique (MART)

The MART technique (5) involves a multiplicative correction to the voxel intensity based on the ratio of the recorded pixel intensity  $P_i$  and the projection of voxel intensities  $\sum_j W_{ij} I_j^k$  from the previous iteration  $k$ :

$$I_j^{k+1} = I_j^k \left( \frac{P_i}{\sum_j W_{ij} I_j^k} \right)^{\mu W_{ij}} \quad (3)$$

where  $\mu$  is a relaxation parameter typically chosen between 0 and 2. Each voxel's intensity is corrected to satisfy one projection or pixel at a time, with a single iteration being completed only after every projection has been considered. This method has been proven to converge to the maximum information based entropy solution (8), which represents the most probable reconstruction based on the recorded projections. Elsinga et al. (4) indicate that this algorithm was preferable to that of additive algebraic reconstruction technique (ART), which was shown to leave artefacts or tracer in the reconstructed field.

#### Improved iterative algorithm for sparse objects (IIASOR)

Li et al. (9) introduced an algorithm referred to as the improved iterative algorithm for sparse object reconstruction, which attempts to select the sparse solution from the multiple intensity fields that can satisfy the recorded projections. The solution method is based on Lagrange duality, which involves performing the following iteration for each projection in each iteration to solve for the dual variable  $\omega_j$ :

$$\omega_j^{k+1} = \omega_j^k + \beta \frac{P_i - \sum_j W_{ij} g_1(\omega_j^k)}{\text{MIN}(\sum_j W_{ij}^2 g_2(\omega_j^k), \gamma)} W_{ij} \quad (4)$$

$$g_1(t) = \begin{cases} \frac{t-1}{\epsilon} & t \geq 1 \\ 0 & t < 1 \end{cases} \quad (5)$$

$$g_2(t) = \begin{cases} \frac{1}{\epsilon} & t \geq 1 \\ 0 & t < 1 \end{cases} \quad (6)$$

where  $\beta$  is a relaxation parameter,  $\epsilon$  is small positive number used to perturb the solution, and  $\text{MIN}(a, b)$  returns the minimum of  $a$  and  $b$  or in this case prevents the denominator from becoming smaller than the small positive constant  $\gamma$ . Equation 4 converges quickly but can become unstable, prompting the switch to the following equation to solve  $\omega_j$  if instability of the solution is observed:

$$\omega_j^{k+1} = \omega_j^k + \frac{P_i - \sum_j W_{ij} g_1(\omega_j^k)}{\frac{1}{\epsilon} \sum_j W_{ij}^2} W_{ij} \quad (7)$$

The initial values of  $\omega_j$  are given by:

$$\omega_j^0 = \sum_i W_{ij} P_i \quad (8)$$

The intensity in each voxel  $I_j$  can then be determined from the values of  $\omega_j$ :

$$I_j^k = g_1(\omega_j^k) \quad (9)$$

#### Adaptive algebraic reconstruction technique (AART)

This technique is an extension to the additive ART algorithm that involves the adaptive adjustment of relaxation parameters during each stage of the reconstruction (10). In the basic additive ART algorithm the each voxels intensity is updated for each projection in each iteration as follows:

$$I_j^{k+1} = I_j^k - \lambda_j^{i,k+1} \left( \sum_j W_{ij} I_j^k - P_i \right) \quad (10)$$

where  $\lambda_j^{i,k+1}$  represents the relaxation parameter for each voxel for a given projection  $i$  and iteration  $k$ . In standard ART this relaxation parameter is either a constant or at least the same for each voxel in a given iteration. In AART this relaxation parameter is instead adjusted for each voxel so that as each projections is considered, the voxels that have a larger intensity contribution to the  $i$ th projection receive the largest correction. This is done via the ratio of the intensity contribution of each voxel  $y_j^k$  to the integration of this intensity contribution along the projection's lines-of-sight  $\sum_j W_{ij} y_j^k$ , where:

$$y_j^k = I_j^k W_{ij} \quad (11)$$

and the relaxation parameter becomes:

$$\lambda_j^{i,k+1} = \frac{y_j^k}{\sum_j W_{ij} y_j^k} \quad (12)$$

#### Simultaneous iterative reconstruction technique (SIRT)

Simultaneous algorithms such as SIRT target a least squares solution to the line-of-sight integral equation, enabling simultaneous consideration of every projection in each iteration. The aim of such an algorithm is to remove the sensitive of the reconstruction to error in each projection (6), requiring  $I_j$  to simultaneously satisfy all projections. The SIRT iteration (2) is shown below:

$$I_j^{k+1} = I_j^k + \lambda^k \frac{\sum_i [W_{ij} (P_i - \sum_h W_{ih} I_h^k) / \sum_h W_{ih}]}{\sum_i W_{ij}} \quad (13)$$

$$\lambda^k = \alpha + \frac{\beta}{k} \quad (14)$$

In this case we have incremented the relaxation parameter as suggested by Bangliang et al. (1), which reduces the correction

in subsequent iterations as the solution is approached. Initial values for  $I_j^0$  are obtained in the same manner as equation 8:

$$I_j^0 = \sum_i W_{ij} P_i \quad (15)$$

### Implementation of the Weighting Matrix

The weighting matrix  $W_{ij}$  used in each of the considered algebraic reconstruction techniques represents the contribution of each voxel to each pixel, with dimension  $m \times n$  where  $m$  is the number of pixel and  $n$  is the number of voxels. A typical  $1280 \times 1024$  pixel camera with a volume of  $1000 \times 1000 \times 200$  voxel grid will therefore require a matrix of  $2.6 \times 10^{14}$  elements for each camera. This matrix is only a factor of the camera orientation and measurement volume configuration and can therefore be calculated once and reused for each set of recorded projections, reducing reconstruction time. Unfortunately for a typical four camera Tomo-PIV setup this will require four matrices of  $2.6 \times 10^{14}$  elements, corresponding to a file-sizes of approximately 520 terra-bytes each.

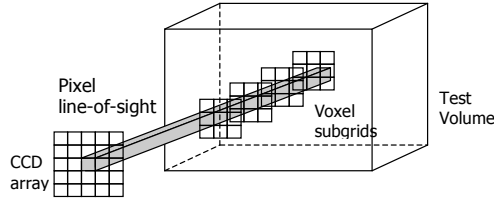


Figure 2: Pixel line-of-sight schematic for a sub-grid weighting matrix.

Each pixel is likely to see only a small portion of the total number of voxels, meaning that the weighting matrix will be very sparse. This lead us to divide the matrix is a series of sub-grids along the viewing direction as shown in figure 2. These sub-grids are sized based on greatest area seen by a pixel in each plane, meaning that if a pixel sees at most a voxel grid of  $vw$  voxels in each plane then the weighting matrix for each camera can be presented by  $m \times nw \times nz$  where  $nz$  is the number of voxels in the line-of-sight direction. For the setup discussed above this would reduce the number of elements to  $2.4 \times 10^9$  per camera. The integration along the line-of-sight of a given pixel  $P_i$  can then be calculated as:

$$P_i = \sum_{nz} \sum_{vw} W_{ij} I_j \quad (16)$$

A transposed form of the weighting matrix can similarly be formed by considering a pixel sub-grid of  $pw$  pixels on the CCD array for each pixel, enabling the initial solution  $I_j^0$  given in equations 8 and 15 to be calculated as:

$$I_j^0 = \sum_{pw} W_{ij} P_i \quad (17)$$

requiring a matrix of  $n \times pw$  elements.

Unfortunately SIRT did not lends itself as well to this approach, resulting in considerable longer calculation times as discussed later.

### Reconstruction Artefacts and Ghost Particles

One common problem that arises in reconstruction of a particle field is the presence of non-zero intensity regions that do not corresponded to actual particle locations (4). Without having

prior knowledge of the true particle location it is not possible to distinguish these regions from true particles, hence the term ghost particles is used. These ghost particles or reconstruction noise originate from there being multiple voxel intensity distributions that are capable of satisfying the camera observed projections (see figure 3). Naturally as more projections are added the number of possible intensity distribution should be reduced, along with the number of ghost particles.

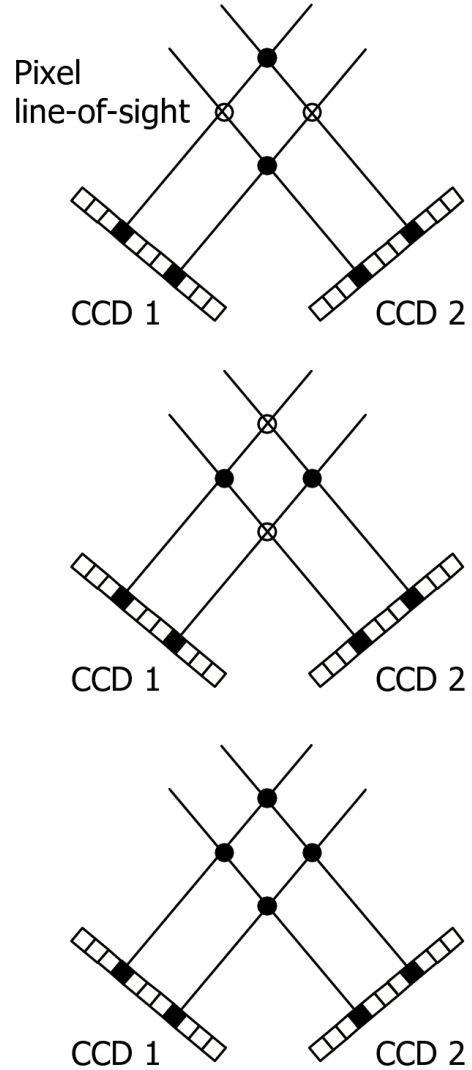


Figure 3: Schematic of particle location ambiguity with multiple possible particle solutions when only 2 projection view angles are taken. Real particle ●; ghost particle ○.

Figure 4 illustrates that as the number of particles increases so to will the number of non-zero projections, which will results in an increase in the possible line-of-sight intersections. The consequence of this is that a greater number of intensity distribution will now satisfy the recorded projection and more ghost particle will be created.

### Reconstruction Simulations Method

In order to assess the application of the previously discussed algorithms to the limited-view particle field reconstruction of Tomo-PIV, particle locations and corresponding projections

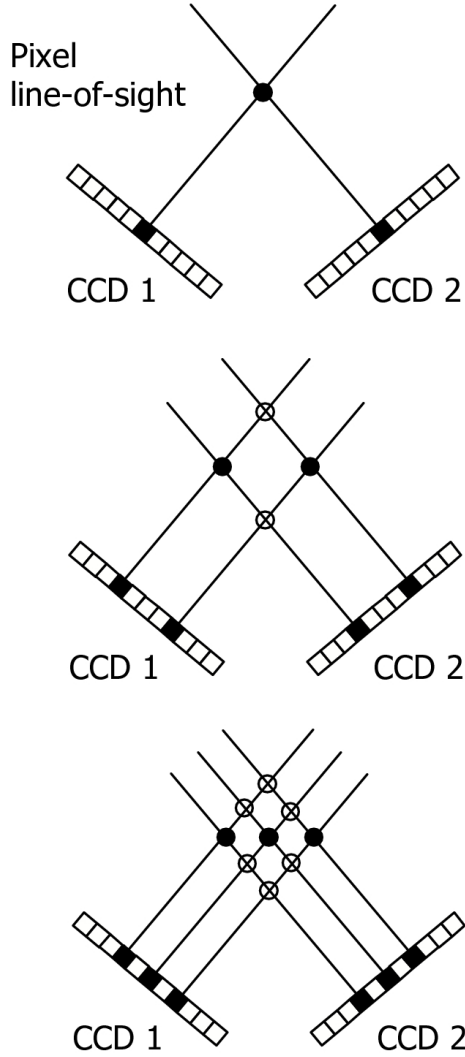


Figure 4: Schematic of increased possible particle solutions as the number of particles is increased. Real particle  $\bullet$ ; ghost particle  $\circ$ .

were simulated. The simulations were carried out under the same condition used by (4), namely a  $1000 \times 200$  voxel plane with three cameras viewing linear projections along the minor dimension of the interrogation region with a 20 deg angular interval between each camera, similar to that shown in figure 1. The projection simulated for each camera consisted of a single row of 1008 pixels. 50 spherical particles with Gaussian intensity distributions with a peak intensity of 4096 were randomly located with a diameter of 3 voxels.

Reconstructions were then undertaken using each of the algorithms with initial intensity distributions and relaxations parameters as in table 1. The CPU processing time for each algorithm, including the time taken to load each weighting matrix and image, was recorded for reconstruction on a two 2.6 GHz dual-core AMD Opteron processors system with 16 GB RAM.

The overall reconstruction quality was evaluated by determining a correlation coefficient  $Q$  between the reconstructed intensity field  $I_{rec,j}$  and the intensity fields consisting of only the Gaus-

MART	IIASOR	AART	SIRT
$I_j^0 = 1$ $\mu = 1$	$\omega_j^0 = \sum_i W_{ij} P_i$ $MIN = 20$ $\beta = 1$ $\epsilon = 0.2$	$I_j^0 = 1$ $\beta = 1$	$I_j^0 = \sum_i W_{ij} P_i$ $\alpha = 1.5$ $\beta = 2.0$

Table 1: Algorithm initial intensity distribution and relaxation parameters

sian spheres  $I_{gaus,j}$ :

$$Q = \frac{\sum_j I_{rec,j} I_{gaus,j}}{\sqrt{\sum_j I_{rec,j}^2 \sum_j I_{gaus,j}^2}} \quad (18)$$

which includes varying in particle intensity, location and the presence of ghost particles.

The relative number of ghost to true particles was determined using a region merging technique. This involved grouping interconnected voxels of non-zero reconstructed intensity into multiple regions, corresponding to particles. These reconstructed regions were then compared against common region locations in the Gaussian sphere intensity field to determine if each region represented a true or ghost particle.

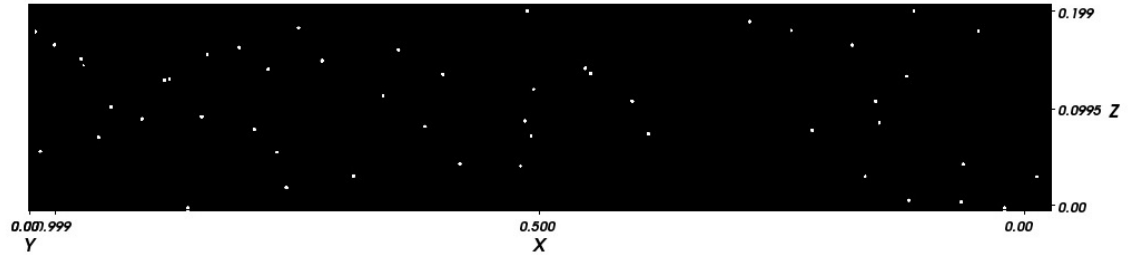
#### Reconstruction Results

An example of the reconstruction after five iterations can be seen figure 5 for each algorithm. In the case of the MART and AART algorithms a high quality reconstruction can be seen after only a small number of iterations. The same can not however be said for the IIASOR and SIRT algorithm. In the case of the IIASOR algorithm the solution shows a large number of small intensity regions with little indication of the original particles. SIRT on the other-hand behaves in a manner similar to that reported by Elsinga et al. (4) when the additive ART algorithm was used, showing the establishment of a series of tracers along the line-of-sight of each non-zero projection.

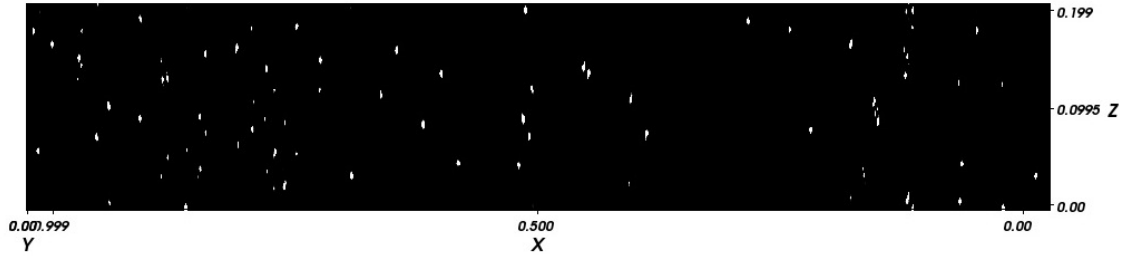
Figure 6 shows the extension to fifteen iterations of the same particle field. These results indicate only a slight improvement for both the MART and AART algorithm. Further progress has been made by both the IIASOR and SIRT algorithms, however each were found to require approximately 50 iteration before a solution of similar quality of the five iterations of MART and AART was achieved.

Plots of the reconstruction coefficient, percentage of ghost particles and CPU process time against the number of iterations are presented in figure 7. Results show that for a limited number of iterations a considerably higher reconstruction coefficient is obtained by both the MART and AART algorithms. These algorithms also produce a much lower number of ghost particles, however this remained on the order of 50%. A comparison of the processing times indicate a slightly faster reconstruction for the AART algorithm, with an apparent slowing of the MART algorithm. This disparity may become more noticeable as the number of voxels is increased.

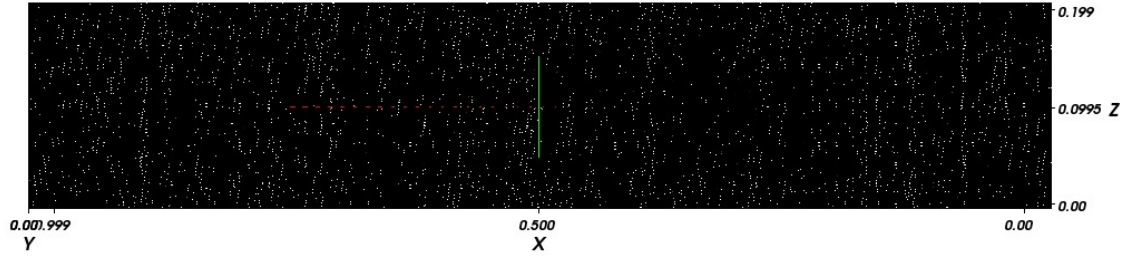
As mentioned previously the use of a sub-grid based weighting matrix did not lend itself to efficient implementation of the SIRT algorithm, owing to the continuous summing along each row of the weighting matrix. This resulted in the SIRT algorithm taking over 30 CPU seconds for a single iteration. For this reason SIRT has been excluded from figure 7c. It should be stated that if some of these summations were to be performed off-line it should be possible to considerably improve the efficiency of the SIRT algorithm. The significantly larger number of iterations required by this algorithm in comparison to MART and AART



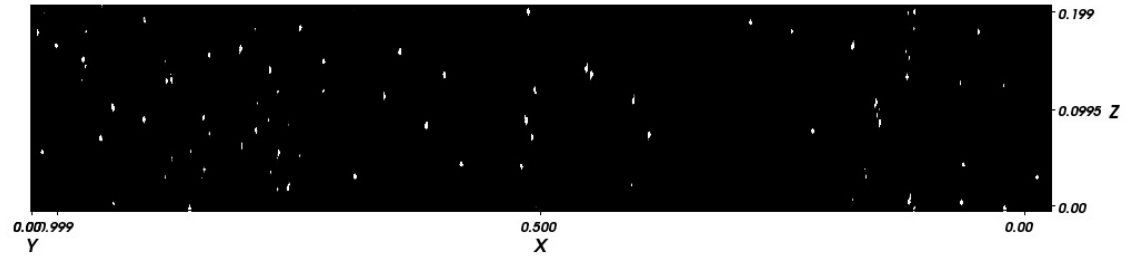
(a)



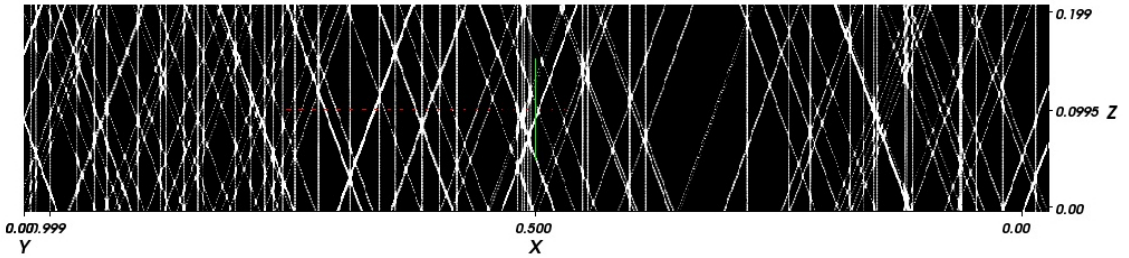
(b)



(c)



(d)



(e)

Figure 5: Reconstruction of simulated projections from 3 cameras at an angular interval of 20 deg for 50 particles in a  $1000 \times 200$  voxel plane, after five iterations. (a) Original Gaussian particles; (b) MART; (c) IIASOR; (d) AART; (e) SIRT.

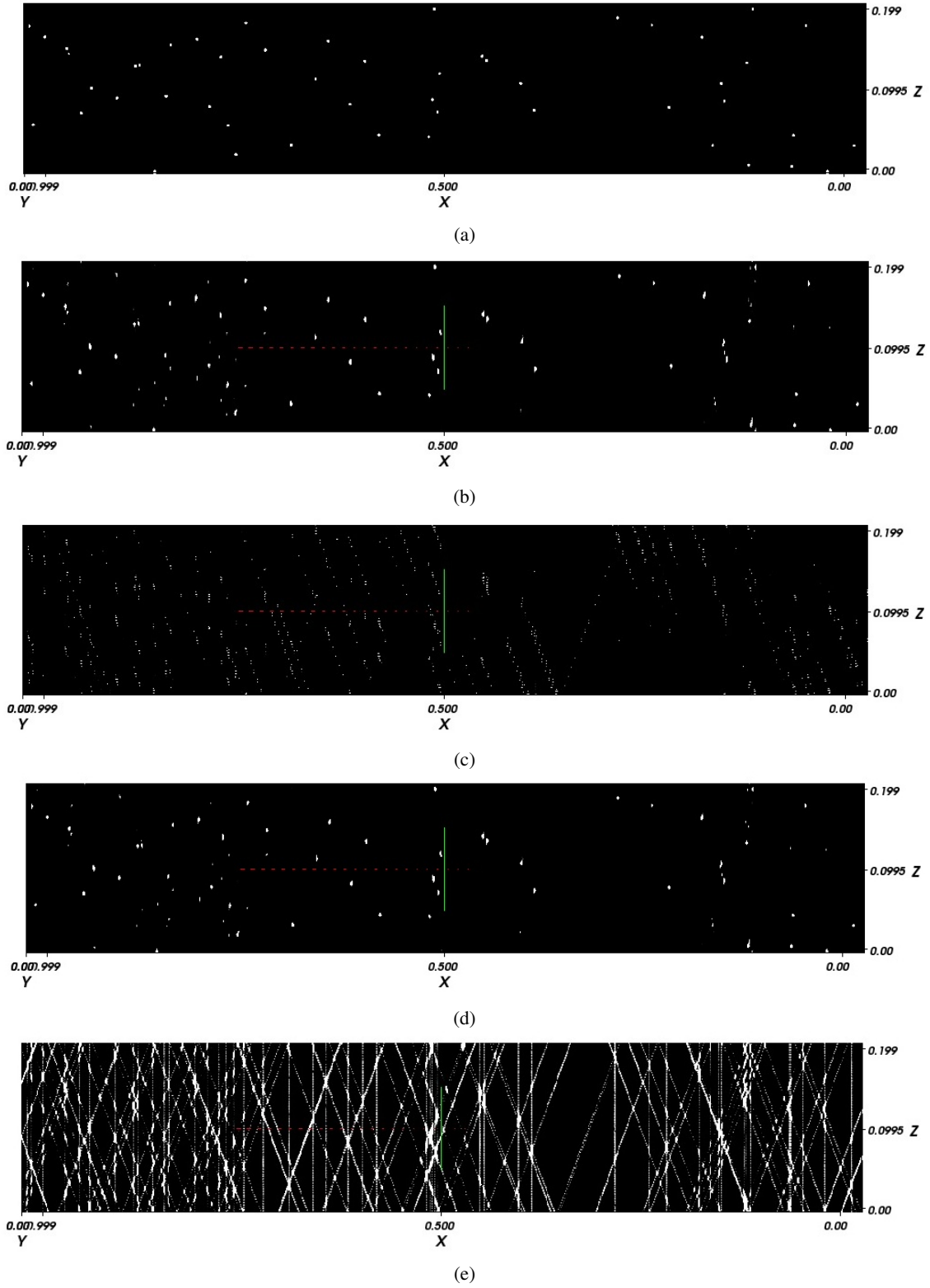


Figure 6: Reconstruction of simulated projections from 3 cameras at an angular interval of 20 deg for 50 particles in a  $1000 \times 200$  voxel plane, after fifteen iterations. (a) Original Gaussian particles; (b) MART; (c) IIASOR; (d) AART; (e) SIRT.

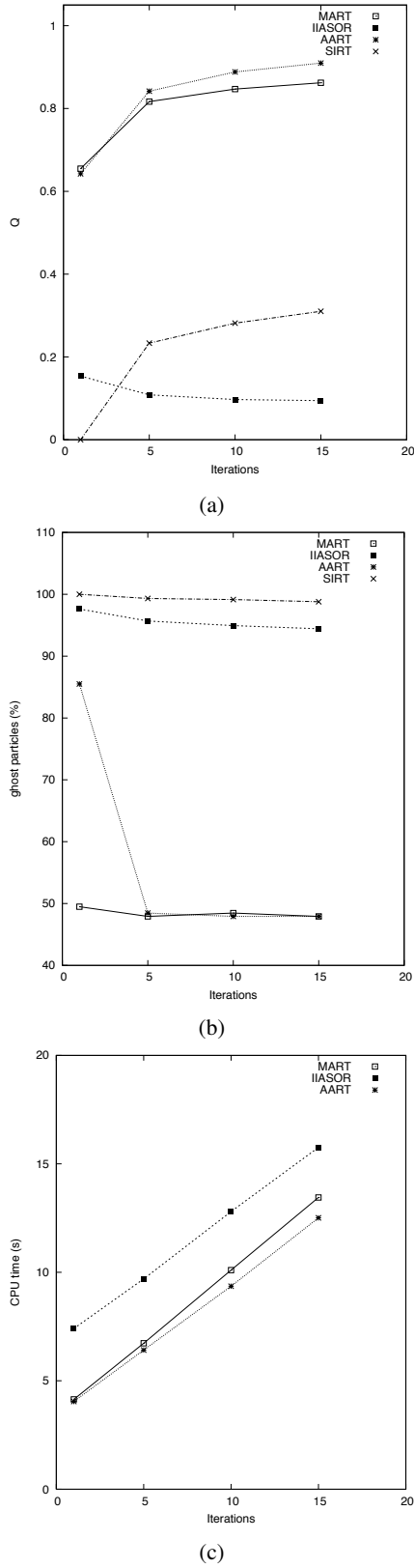


Figure 7: Reconstruction quality for different numbers of iterations of simulated projections from 3 cameras at an angular interval of 20 deg for 50 particles in a  $1000 \times 200$  voxel plane. (a) Correlation coefficient; (b) percentage of ghost particles; (c) CPU processing time.

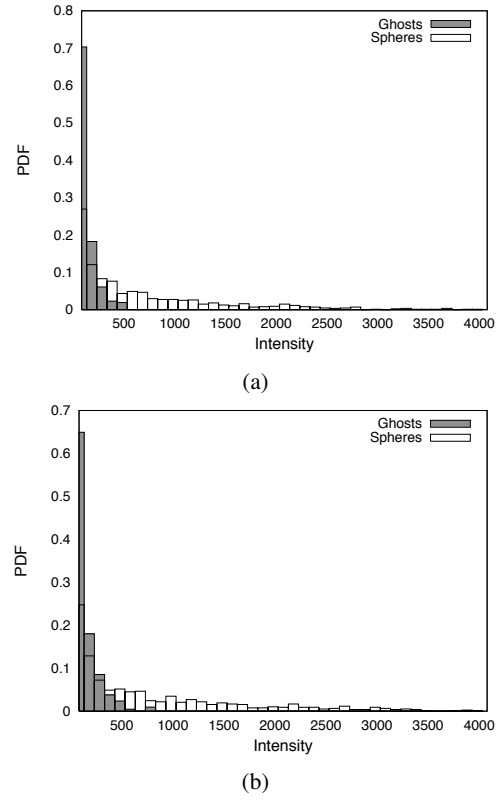


Figure 8: Probability density function of true and ghost particles. (a) MAART; (b) AART.

meant that further optimisation of the SIRT algorithm was not performed in this paper.

A comparison of the probability density function (PDF) for the intensity of true and ghost particles generated by both the MART and AART algorithms can be seen in figure 8. While both algorithms were shown to produce ghost particle on the order of 50% it is clear that most of these particles are of much lower intensity than the true reconstructed particles. It should therefore be possible to remove many of these ghost particle by careful thresh-holding of the reconstructed intensity field.

## Conclusions

A series of iterative algebraic reconstructed algorithms are specifically tested for their applicability to Tomo-PIV particle field reconstruction. Results indicate that the MART and AART algorithms provides higher quality reconstruction for fewer iterations and less processing time than either the IASOR or SIRT techniques. An efficient means of implementing the weighting matrix is also discussed.

## Acknowledgements

The support of the Australian Research Council of this research is gratefully acknowledged. C.H. Atkinson was supported by an Australian Postgraduate Scholarship while undertaking this research.

\*

## References

- [1] Bangliang, S., Yiheng, Z., Lihui, P., Danya, Y. and Baofen, Z., The use of simultaneous iterative reconstruction technique for electrical capacitance tomography, *Chemical Engineering Journal*, **77**, 2000, 37–41.
- [2] Benson, T. M. and Gregor, J., Modified simultaneous iterative reconstruction technique for faster parallel computation, in *IEEE Nuclear Science Symposium Conference Record*, 2005, 2715–2718, 2715–2718.
- [3] Bracewell, R. N., Strip integration in radio astronomy, *Australian Journal of Physics*, **9**, 1956, 198–217.
- [4] Elsinga, G. E., Scarano, F., Wieneke, B. and van Oudheusden, B. W., Tomographic particle image velocimetry, *Experiments in Fluids*, **41**, 2006, 933–947.
- [5] Gordon, R., Bender, R. and Herman, G. T., Algebraic reconstruction techniques (art) for three-dimensional electron microscopy and x-ray photography, *J. Theor. Biol.*, **29**, 1970, 471.
- [6] Herman, G. T. and Lent, A., Iterative reconstruction algorithms, *Compt. Biol. Med.*, **6**, 1976, 273–294.
- [7] Lamarche, F. and Leroy, C., Evaluation of the volume of intersection of a sphere with a cylinder by elliptic integrals, *Computer Physics Communications*, **59**, 1990, 359–369.
- [8] Lent, A., Maximum entropy and the multiplicative art, in *Proc. Conf. Image Analysis and Evaluation, SPSE*, Toronto, 1976.
- [9] Li, M., Kudo, H., Hu, J. and Johnson, R. H., Improved iterative algorithm for sparse object reconstruction and its performance evaluation with micro-ct data, *IEEE Transactions on Nuclear Science*, **51**, 2004, 659–666.
- [10] Lu, W. and Yin, F., Adaptive algebraic reconstruction technique, *Med. Phys.*, **31**, 2004, 3222–3230.
- [11] Oldendorf, W. H., Solated flying spot detection of radiodensity discontinuities-displaying internal structural pattern of complex object, *IRE - Transactions on Bio-Medical Electronics, BME*, **8**, 1961, 68–71.
- [12] Radon, J., Uber die bestimmung von funktionen durch ihre integralwerte langs gewisser mannigfaltigkeiten, *Ber. Sachsische Akad. Wiss., Leipzig, Math.-Phys.*, **69**.